






## Bayesian uncertainty quantification on nuclear level-density data and their impact on $(p, \gamma)$ reactions of astrophysical interest

A. Chalil <sup>\*</sup>, C. Ducoin, O. Stézowski , N. Millard-Pinard, J. Dudouet , Y. Demane, and M. Chamseddine   
*Université Lyon, Université Claude Bernard Lyon 1, CNRS/IN2P3, IP2I Lyon, F-69622 Villeurbanne, France*

 (Received 17 February 2024; revised 7 May 2024; accepted 22 July 2024; published 1 August 2024)

The  $p$  process nucleosynthesis is responsible for the synthesis of 35 neutron-deficient nuclei from  $^{35}\text{Se}$  to  $^{196}\text{Hg}$ . An important input that can affect the modeling of this process is the nuclear level density at the relevant excitation energies of the nuclei involved in the reaction network. The OSLO method has been extensively used for the measurement of level densities in excitation energies of several MeV. In this work, Bayesian optimization has been used in order to estimate the 95% credible intervals for the parameters of two level-density models optimized on the OSLO data. These uncertainties are then propagated on the cross sections of  $(p, \gamma)$  reactions leading to the compound nuclei  $^{105,106}\text{Pd}$  and  $^{105,106}\text{Cd}$  inside the astrophysically relevant energy range. Imposing constraints in this region of the isotopic chart is important for network calculations involving the nearby  $p$  nuclei  $^{102}\text{Pd}$  and  $^{106}\text{Cd}$ . We discuss the reduction of the range of cross sections due to the uncertainties arising from the level-density data compared to the range of the six default level-density models available in TALYS and we highlight the need for level-density data inside the astrophysically relevant energy ranges.

DOI: [10.1103/PhysRevC.110.024602](https://doi.org/10.1103/PhysRevC.110.024602)

### I. INTRODUCTION

Thirty-five neutron-deficient nuclei, from  $^{94}\text{Se}$  to  $^{196}\text{Hg}$  cannot be created by the  $s$  and  $r$  processes, which are based on neutron capture and are responsible for the synthesis of the bulk of elements heavier than iron [1,2]. The  $s$  process, whose most probable astrophysical site are the AGB stars [3], runs close to the valley of stability, creating stable nuclei until Bismuth. On the contrary, the  $r$  process rapidly deviates from the stable region, flowing to neutron-rich nuclei far from stability, in order to allow for subsequent  $\beta^-$  decays to form neutron-rich nuclei. The kilonova signal [4], observed in 2017 by a neutron star merger, has greatly contributed to the question of the astrophysical site of the  $r$  process [5].

For the creation of the nuclei on the neutron-deficient side of the nuclear chart, another process had to be introduced in order to explain their existence in our solar system. This process is called the  $p$  process, and when photodisintegration reactions are dominant, the term  $\gamma$  process is also used [6]. Candidates for the astrophysical sites of the  $p$  process are the supernovae of type II and type Ia [7–9].

The modeling of the reaction network of the  $\gamma$  process consists of around 20 000 reactions involving approximately 2000 nuclei below a mass number of  $A \leq 210$  [6]. Important reactions in this network are photodisintegration reactions such as  $(\gamma, n)$ ,  $(\gamma, p)$ ,  $(\gamma, \alpha)$ , as well as their inverse ones  $(n, \gamma)$ ,  $(p, \gamma)$ ,  $(\alpha, \gamma)$ . For the case of radiative proton capture,

their cross-section values lie usually in the range of 1–100  $\mu\text{b}$  inside the Gamow window [6]. Such low cross sections can be notably challenging to measure experimentally. If the target nucleus is stable, then measurements can be performed using a proton beam on a preferably isotopic target, with the latter to minimize any beam induced background on the  $\gamma$  spectra, using various techniques [10–12]. A highly efficient detecting setup is also necessary to counter the low values of the cross sections. On the other hand, if the target nucleus is not stable, then inverse kinematics measurements with radioactive beams can provide a solution as shown in a recent study [13]. However, the low values of these cross sections can pose again a significant challenge, which could lead to relatively large uncertainties. Attempts have also been made in the past using the GANIL Wien filter [14].

Due to the scarcity of experimental cross sections, the calculations of the relevant reaction rates rely heavily on Hauser-Feshbach statistical model calculations [15]. Within the Hauser-Feshbach model, quantities such as optical model potentials (OMPs), nuclear level densities (NLDs), and  $\gamma$ -strength functions ( $\gamma$ SFs) are parameters that can significantly influence the reaction cross sections and subsequently the reaction rates in the respective stellar environments.

At relatively low energies inside the Gamow window, and close to the low-mass  $p$  nuclei, the OMPs are the most sensitive parameter in cross-section calculations [16]. However, large uncertainties seem to arise at higher energies due to the unknown NLDs and  $\gamma$ SFs. These two parameters can be significantly constrained, when experimental data are available by the OSLO method [17]. Data obtained by this method can help constrain NLD and  $\gamma$ SFs, which have a significant impact on the cross sections relevant to the  $\gamma$ -process reaction network.

<sup>\*</sup>Present address: CEA, DES, IRESNE, Nuclear Measurement Laboratory, F-13108 Saint-Paul-lez-Durance, France; achment.chalil@cea.fr

In this work, we focus on the impact of NLD uncertainties on the radiative-capture cross sections for several important reactions for the  $\gamma$  process [18,19]. In particular, the present work is concentrated on the radiative proton-capture reactions which can happen in the vicinity of the  $p$  nuclei  $^{102}\text{Pd}$  and  $^{106}\text{Cd}$ . The reactions  $^{104,105}\text{Ag}(p, \gamma)^{105,106}\text{Cd}$  and  $^{104,105}\text{Rh}(p, \gamma)^{105,106}\text{Pd}$  are studied in the present work in terms of their proton-capture cross sections and their uncertainty after optimization of the corresponding NLD data. Cross-section data for these reactions still remain unmeasured, as such data would be also hard to obtain, in particular with stable beams, as the target nuclei are not stable. However, experimental data on NLDs exist for those nuclei [20], making it possible to constrain the model calculations for the radiative proton-capture cross sections.

The cross sections and the relevant reaction rates of the reactions  $^{104,105}\text{Rh}(p, \gamma)^{105,106}\text{Pd}$  can have an influence on the synthesis of the  $p$  nucleus  $^{102}\text{Pd}$ . As shown in Ref. [16], this nucleus is underproduced in model calculations. The aforementioned reactions are happening on the vicinity of this nucleus and their cross sections are still not measured. This is due to the difficulty in using stable beams on the unstable isotopes  $^{104,105}\text{Rh}$ , as well as the challenge on producing the corresponding radioactive beams for inverse-kinematics measurements. Until today, the only measurements on radiative-capture reactions involving Pd isotopes have been performed in Refs. [21,22]. It is thus important to take advantage of the available level-density data [23] and attempt to constrain cross sections of neighboring reactions.

Furthermore, the Cd isotopic chain hosts a  $p$  nucleus ( $^{106}\text{Cd}$ ) whose abundance is significantly underproduced by astrophysical models [16], as in the case of  $^{102}\text{Pd}$ . Proton-capture cross sections studies reaching  $^{108}\text{Cd}$  are more accessible due to the existence of the stable target  $^{107}\text{Ag}$ . These cross sections have been studied extensively in Refs. [24,25] and have sufficiently constrained the cross-section ranges inside the Gamow window. On the other hand, for the case of  $^{105,106}\text{Cd}$ , similar data are nonexistent because of the lack of stable targets. In Ref. [19], theoretical calculations predict high degree of competition between the reaction  $^{104}\text{Ag}(p, \gamma)^{105}\text{Cd}$  and  $^{105}\text{Ag}(n, \gamma)^{106}\text{Cd}$ . It is thus necessary to take advantage of the level-density data for  $^{105,106}\text{Cd}$  and attempt to constrain the range of cross sections of the proton capture reactions  $^{104}\text{Ag}(p, \gamma)^{105}\text{Cd}$  and  $^{105}\text{Ag}(p, \gamma)^{106}\text{Cd}$  by optimizing the BSFG and HFB + comb models on the OSLO data for these isotopes [26].

Bayesian optimization has been used in the present work in order to estimate 95% credible intervals on the level-density data which are available at the OSLO database of experimental NLDs [20]. The phenomenological Back-shifted Fermi gas model (BSFG) [27,28], as well as the semimicroscopic level densities derived from Hartree-Fock-Bogoliubov plus the combinatorial (HFB + comb) method [29] have been used for the estimation of these intervals. Then these intervals have been used in order to calculate the corresponding cross sections inside the Gamow window [30]. The nuclear reaction code TALYS [31] has been used to calculate all values for the theoretical NLDs and cross sections presented in this work.

TABLE I. Table of reactions relevant to the  $p$  process studied in this work. The Gamow window (GW) corresponds to stellar temperatures of  $T_9 = 1.7\text{--}3.3$ . The references of the level-density experimental data are also given.

Reaction	$Q$ value (MeV)	GW (MeV)	$E_x$ (MeV)	Ref.
$^{104}\text{Rh}(p, \gamma)^{105}\text{Pd}$	8.748	1.54–4.55	10.28–13.30	[23]
$^{105}\text{Rh}(p, \gamma)^{106}\text{Pd}$	9.345	1.54–4.55	10.88–13.89	[23]
$^{104}\text{Ag}(p, \gamma)^{105}\text{Cd}$	6.506	1.59–4.67	8.10–11.17	[26]
$^{105}\text{Ag}(p, \gamma)^{106}\text{Cd}$	7.350	1.59–4.67	8.94–12.02	[26]

It is important to note that only the uncertainties arising from the NLDs are considered in this work. Concerning the OMPs and  $\gamma$ SF models, the Koning-Delaroche potential [32] and the Kopecky-Uhl standard Lorentzian [33] have been used respectively, using the default values of their parameters in TALYS. Furthermore, this work does not consider the systematic uncertainties arising due to the model dependent normalization of the level-density data [34]. While the latter can give rise to important deviations, this work considers the data as given in the OSLO database [35], along with the level-density values at the neutron separation energy for each target nucleus given in Refs. [23,26]. The normalization issue could be avoided by the newly developed shape method [36] in the future, which introduces a model-independent normalization of the level-density data.

Radiative-proton capture reactions proceed mainly via the compound nucleus mechanism in the Gamow window. For the scenario of the synthesis of the  $p$  nuclei during the explosive phase of a type II supernova, where the temperature is in the range  $T_9 = 1.7\text{--}3.3$  [6], this window ranges from 1.2 to 6.4 MeV for the whole reaction network and in the center of mass for proton-capture reactions. In this range, the reactions proceed by the compound nucleus mechanism [37,38]. In Table I, the Gamow window, as well as the  $Q$  values and excitation energies for the compound nuclei formed after the reactions  $^{104,105}\text{Ag}(p, \gamma)^{105,106}\text{Cd}$  and  $^{104,105}\text{Rh}(p, \gamma)^{105,106}\text{Pd}$ , are given along with the corresponding references of the NLD data.

## II. MODELS AND METHODS

### A. The Back-shifted Fermi gas model

The first model that will be used in the present work in order to constrain the level densities is the phenomenological Back-shifted Fermi gas model (BSFG) [27]. The advantage of this phenomenological model allows for the optimization of its parameters along the whole energy range, contrary to the Gilbert-Cameron model [39], which is essentially a combination of the constant-temperature model at low excitation energies and the Fermi gas model at higher excitation energies. Furthermore, the OSLO data used in this work have been renormalized using this model [35]. In addition, the relevant excitation energies for proton capture relevant to the  $p$  process are in the range where a Fermi gas description is more appropriate.

In the BSFG model, which is implemented in the TALYS code, the level density is given by the formula:

$$\rho_{\text{tot}}(U) = \frac{1}{\sqrt{2\pi}\sigma} \frac{\sqrt{\pi} \exp(2\sqrt{aU})}{12 a^{1/4} U^{5/4}}. \quad (1)$$

where  $\sigma$  is the spin-cutoff parameter. The quantity  $U$  is connected with the excitation energy  $E_x$ :

$$U = E_x - \chi \frac{12}{\sqrt{A}} - \delta^{\text{BSFG}}, \quad (2)$$

where  $\chi = -1, 0, +1$  for odd-odd, odd-even, and even even nuclei, respectively;  $A$  is the mass number of the nucleus; and  $a, \delta^{\text{BSFG}}$  are free parameters. The posterior distributions of these parameters will be sampled in order to estimate the credible intervals for each parameter. It is to be noted that while the parameter  $a$  can be treated as energy dependent to account for shell effects, no energy dependence is taken into account in the present work.

### B. The Skyrme-Hartree-Fock Bogoliubov plus combinatorial model

The Skyrme-Hartree-Fock Bogoliubov plus combinatorial model (HFB + comb) is a microscopic model used to calculate the level densities for excitation energies up to 200 MeV [29]. These level densities are available in TALYS in tabulated format.

Within TALYS, the possibility of adjusting these microscopic level densities  $\rho_{\text{tab}}$  to the experimental data has also been added by using two-parameter scaling function of the form [31]:

$$\rho(E_x, J, \pi) = \exp(c\sqrt{E_x - \delta^{\text{HFB}}}) \rho_{\text{tab}}(E_x - \delta^{\text{HFB}}, J, \pi), \quad (3)$$

where  $E_x$  is the excitation energy;  $J$  and  $\pi$  are the spin and parity of the excited state; and  $c, \delta^{\text{HFB}}$  are parameters that play a similar role as the parameters  $a$  and  $\delta^{\text{BSFG}}$  of the previously mentioned BSFG model.

Using the available experimental data given by the OSLO database, it is thus possible to calculate the posterior distributions for the parameters  $c, \delta^{\text{HFB}}$  of the scaling function and estimate the relevant credible intervals. A comparison of the relevant credible intervals with the ones of the BSFG model is also interesting in order to see how the uncertainties vary depending on the model choice.

### C. Bayesian optimization

Bayesian optimization is a statistical method that can optimize the free parameters of a model in order to describe a dataset. In nuclear reaction theory, this approach has been successfully used for constraining OMPs for nucleon transfer reactions [40–44]. It has also been argued that the uncertainties obtained by the Bayesian approach represent more accurately the real uncertainties compared to the uncertainties obtained by frequentist approaches [45].

Bayesian optimization is based on Bayes's theorem:

$$P(H|D; \bar{\theta}) = \frac{P(H; \bar{\theta})P(D|H; \bar{\theta})}{P(D; \bar{\theta})}. \quad (4)$$

TABLE II. Prior distributions for parameters  $a, \delta^{\text{BSFG}}$  of the BSFG model and  $c, \delta^{\text{HFB}}$  of the scaled HFB+comb model [Eq. (4)]. An uninformative Gaussian prior is used in all cases. The means  $a_M, \delta_M^{\text{BSFG}}, c_M, \delta_M^{\text{HFB}}$  and their standard deviations  $\sigma_a, \sigma_{\delta^{\text{BSFG}}}, \sigma_c, \sigma_{\delta^{\text{HFB}}}$  are tabulated. See text for details.

Isotope	$a_M$	$\delta_M^{\text{BSFG}}$	$\sigma_a$	$\sigma_{\delta^{\text{BSFG}}}$	$c_M$	$\delta_M^{\text{HFB}}$	$\sigma_c$	$\sigma_{\delta^{\text{HFB}}}$
$^{105}\text{Pd}$	11.93	0.17	119.3	17	0	0	10	10
$^{106}\text{Pd}$	12.03	0.17	120.3	17	0	0	10	10
$^{105}\text{Cd}$	11.93	0.17	119.3	17	0	0	10	10
$^{106}\text{Cd}$	12.03	0.17	120.3	17	0	0	10	10

Here  $P(H; \bar{\theta})$  is a *prior* distribution that expresses our prior hypothesis  $H$  of the distributions of the model parameters  $\bar{\theta}$ , without the information of the dataset  $D$  that we want to study. Next,  $P(D|H; \bar{\theta})$  is the *likelihood* function, which expresses the degree of probability that our model correctly describes the dataset, while  $P(D; \bar{\theta})$  is the *model evidence*, which expresses the sum of probabilities of all possible hypotheses. The model evidence is essentially a scaling factor and does not vary over the parameter space. This distribution in general cannot be calculated analytically, but it is possible to sample the distribution using Markov-chain Monte Carlo (MCMC) methods. The above three distributions give the *posterior* distribution  $P(H|D; \bar{\theta})$ , which expresses the probability distribution of the parameters  $\bar{\theta}$  after the information obtained from the dataset.

As previously mentioned, due to the difficulty in calculating the evidence analytically, the posterior distributions in Eq. (4) have to be sampled. For this work we have used the Goodman and Weare ensemble sampler [46] with the relevant software package EMCEE [47]. The sampler was coupled with the TALYS code for the calculation of the theoretical level-density values (see Python script in the Supplemental Material [48]).

For the BSFG model, we have used as prior distributions wide Gaussians of mean equal to the values derived from systematics [31]. The standard deviation of these Gaussians is 100 times their mean values, in order to fully explore the parameter space (see Sec. III C). For the HFB + comb model we have used priors centered at 0 and a standard deviation equal to 10, which is the limit that TALYS imposes. Table II summarizes all the Gaussian priors and their standard deviations used for each isotope in the present work. The likelihood is calculated from the relation:

$$P(D|H; \bar{\theta}) = \prod_{i=1}^N \frac{1}{\sigma_i \sqrt{2\pi}} \exp \left\{ -\frac{1}{2} \frac{[\rho_i^{\text{th}}(\bar{\theta}) - \rho_i^{\text{exp}}]^2}{\sigma_i^2} \right\}, \quad (5)$$

where  $N$  is the number of data points;  $\rho_i^{\text{th}}(\bar{\theta})$  is the level density given by the model, which is a function of a given number of model parameters  $\bar{\theta}$ ;  $\rho_i^{\text{exp}}$  is the experimental value and  $\sigma_i^2$  is calculated from [49,50]:

$$\sigma_i^2 = \sigma_{\rho,i}^2 + (\rho_i^{\text{th}})^2 \times \exp(\ln f^2), \quad (6)$$

where  $\sigma_{\rho,i}$  are the measurement errors of the experimental data; and the positive parameter  $f$  expresses any unknown

TABLE III. Posterior distributions for the parameters  $a$ ,  $\delta^{\text{BSFG}}$  and  $\ln f$  of the BSFG model. The 95% high-density intervals ( $a_1$ ,  $a_2$ ), ( $\delta_1^{\text{BSFG}}$ ,  $\delta_2^{\text{BSFG}}$ ) and ( $\ln f_1^{\text{BSFG}}$ ,  $\ln f_2^{\text{BSFG}}$ ) are given.

Isotope	$^{105}\text{Pd}$	$^{106}\text{Pd}$	$^{105}\text{Cd}$	$^{106}\text{Cd}$
$a_1$	12.03	11.54	10.67	10.9
$a_2$	12.61	12.12	11.28	11.38
$\delta_1^{\text{BSFG}}$	-1.07	-1.08	-1.02	-1.03
$\delta_2^{\text{BSFG}}$	-0.90	-0.88	-0.78	-0.85
$\ln f_1^{\text{BSFG}}$	-2.23	-1.18	-1.77	-1.20
$\ln f_2^{\text{BSFG}}$	-1.58	-0.74	-1.13	-0.75

inaccuracies/noise between the models and the data. Since these inaccuracies are not known, this parameter will be optimized at the same time with the other model parameters to obtain a posterior distribution. For the parameter  $f$ , always a flat prior will be used between  $\ln f = -10$  and  $\ln f = 1$ .

### III. RESULTS AND DISCUSSION

#### A. The reactions $^{104,105}\text{Rh}(p, \gamma)^{105,106}\text{Pd}$

The posterior distributions optimized for the level-density parameters  $a$ ,  $\delta^{\text{BSFG}}$  of the BSFG model, as well as for the natural logarithm of the parameter  $f$ , are shown in Fig. 1 and their numerical values are tabulated in Table III. The same are shown for the HFB + comb model in Fig. 2 and in Table IV. The correlations between the three parameters of each model are also shown in the same figures. Although not present in every case, there seems to be a correlation between the parameters  $a$  and  $\delta^{\text{BSFG}}$  for the BSFG model and between the parameters  $c$  and  $\delta^{\text{HFB}}$ . The complex ‘‘interaction’’ between the priors and the likelihood makes it difficult to pinpoint the reason; however, it seems that there is more correlation for the cases of odd-even nuclei, where the datasets of the level densities do not show strong oscillating behavior at low energies. The strong correlations could be an indication that the model is unnecessarily complex and thus not the most appropriate one for the description of the odd-even datasets. Additionally, no correlations are observed with the parameter  $f$ .

The 95% credible intervals can be calculated directly from the posterior distributions and they can then be compared

TABLE IV. Posterior distributions for the parameters  $c$ ,  $\delta^{\text{HFB}}$  and  $\ln f$  of the HFB+comb model. The 95% high-density intervals ( $c_1$ ,  $c_2$ ), ( $\delta_1^{\text{HFB}}$ ,  $\delta_2^{\text{HFB}}$ ) and ( $\ln f_1^{\text{HFB}}$ ,  $\ln f_2^{\text{HFB}}$ ) are given.

Isotope	$^{105}\text{Pd}$	$^{106}\text{Pd}$	$^{105}\text{Cd}$	$^{106}\text{Cd}$
$c_1$	-0.42	-0.39	-0.1	0.47
$c_2$	-0.13	-0.23	0.09	0.56
$\delta_1^{\text{HFB}}$	-1.23	0.05	-0.63	0.32
$\delta_2^{\text{HFB}}$	-0.85	0.22	-0.39	0.39
$\ln f_1^{\text{HFB}}$	-2.08	-1.59	-2.05	-1.58
$\ln f_2^{\text{HFB}}$	-1.49	-1.09	-1.41	-1.06

with the level-density data. The comparisons are shown in Figs. 3(a) and 3(b), together with the calculated cyan and red bands corresponding at the 95% of the credible intervals for the BSFG and HFB + comb models, respectively.

Using the 95% credible intervals, the corresponding range of radiative proton-capture cross sections of the reactions  $^{104,105}\text{Rh}(p, \gamma)^{105,106}\text{Pd}$  can be calculated using TALYS. The results for both the BSFG and the HFB + comb models are shown in Figs. 3(c) and 3(d). It has to be noted that although the ideal approach would be to simultaneously infer NLDs and cross sections on the level-density data, a separate cross-section calculation is performed using the 95% credible intervals of the NLDs. This was done in order to avoid a very computationally expensive calculation, as for each sample the TALYS code would have to compute simultaneously OMPs, NLDs, and  $\gamma$ SFs in order to give the cross-section results.

For the case of  $^{105}\text{Pd}$ , the model uncertainties are smaller for the BSFG model reaching approximately a difference up to factor of 2, compared to the scaled HFB + comb model. This is not the case for the isotope  $^{106}\text{Pd}$ , where not only the uncertainty intervals are smaller but there is a noticeably very good description of the HFB.+comb on the lower energy parts below 3 MeV. The ‘‘oscillating’’ behavior in these energy range is nicely reproduced and the calculated uncertainties contain well the datasets. It is important to note that in the case of the BSFG model, this low energy behavior  $^{106}\text{Pd}$  is enlarging the credible intervals in this region, leading to larger uncertainties.

When attempting to extrapolate to the Gamow Window (gray shaded area in the figures), the two models and their uncertainties can differ by approximately a factor of 4.5. In particular for the case of  $^{105}\text{Pd}$ , the maximum difference can reach even almost half an order of magnitude. The reason for this could be traced on the different behavior of the models at higher energies. The lack of experimental level-density data at energies inside the Gamow window is also a factor, highlighting a necessity for measurements at higher excitation energies. These uncertainties are propagated to the cross sections, which are relatively smaller at low energies. This is expected, as at these energies, the cross section depends mainly on the OMPs and not on the level density.

#### B. The reactions $^{104}\text{Ag}(p, \gamma)^{105}\text{Cd}$ and $^{105}\text{Ag}(p, \gamma)^{106}\text{Cd}$

The same procedure is followed as for the previously described Pd isotopes. The posterior distributions and the correlations of the BSFG model parameters  $a$ ,  $\delta^{\text{BSFG}}$  and  $\ln f$  and the HFB + comb model parameters  $c$ ,  $\delta^{\text{HFB}}$  and  $\ln f$  for the isotopes  $^{105,106}\text{Cd}$  are shown in Figs. 1 and 2 and tabulated in Tables III and IV, respectively.

The calculated level densities and the cross sections of the reactions  $^{104,105}\text{Ag}(p, \gamma)^{105,106}\text{Cd}$  are compared with the data in Figs. 4(a) and 4(b) for the BSFG model and for the HFB + comb model. The range of uncertainties of the NLDs from the two models is quite similar for the isotope  $^{105}\text{Cd}$ . On the contrary, for the isotope  $^{106}\text{Cd}$  the uncertainties are significantly smaller for the HFB + comb model, and the description of the low-energy data is very accurate. These

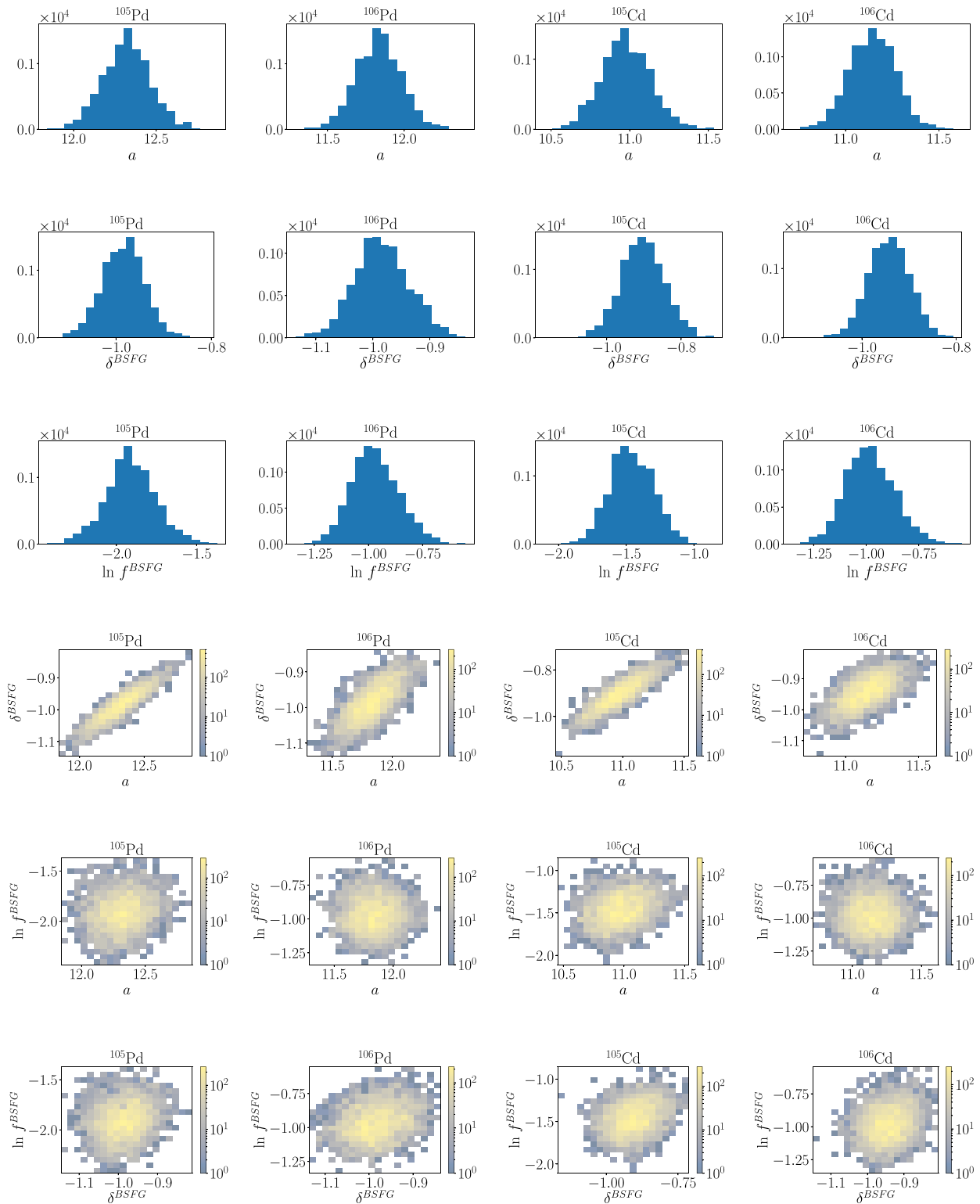


FIG. 1. Posterior distributions of the parameters  $a$ ,  $\delta^{BSFG}$  and  $\ln f^{BSFG}$  by optimizing the BSFG model on the OSLO data for the isotopes  $^{105,106}\text{Pd}$  and  $^{105,106}\text{Cd}$ . Each column is associated with the isotopes and each row with the parameters. The correlations between the parameters are also shown. See text for details.

results point out that uncertainties can significantly depend on the choice of the model. It is also noticeable that the two models tend to diverge at excitation energies higher than 5 MeV, where the uncertainties of the data are higher. This is

expected, as the uncertainties act as a weight in the likelihood [Eq. (5)], resulting in larger divergence between model and data in this excitation energy range. The cross sections of the reactions  $^{104}\text{Ag}(p, \gamma)^{105}\text{Cd}$  and  $^{105}\text{Ag}(n, \gamma)^{106}\text{Cd}$  are shown

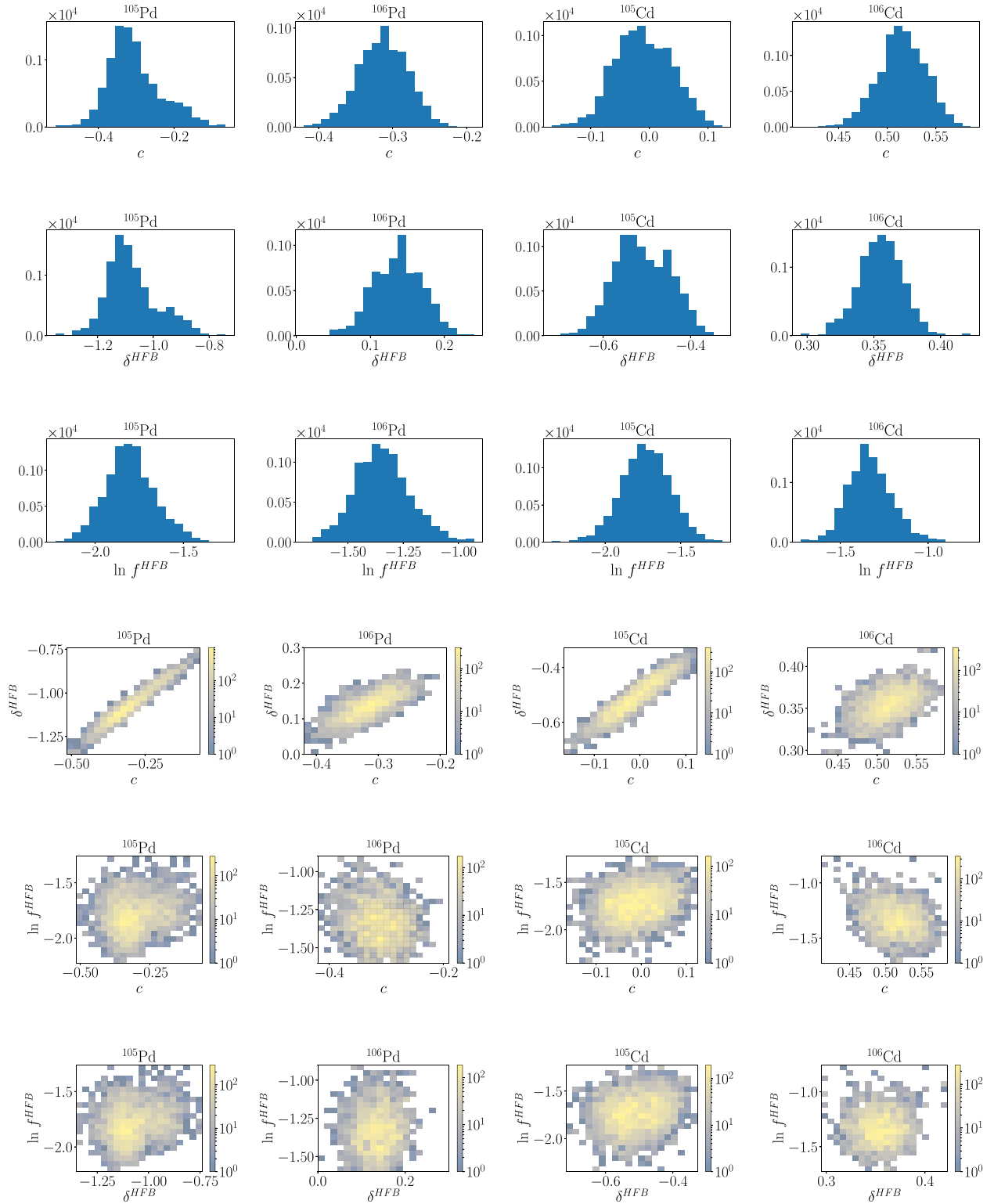


FIG. 2. Posterior distributions of the parameters  $c$ ,  $\delta^{HFB}$  and  $\ln f^{HFB}$  by optimizing the scaling function of Eq. 3 for the HFB + comb model on the OSLO data for the isotopes  $^{105,106}\text{Pd}$  and  $^{105,106}\text{Cd}$ . Each column is associated with the isotopes and each row with the parameters. The correlations between the parameters are also shown. See text for details.

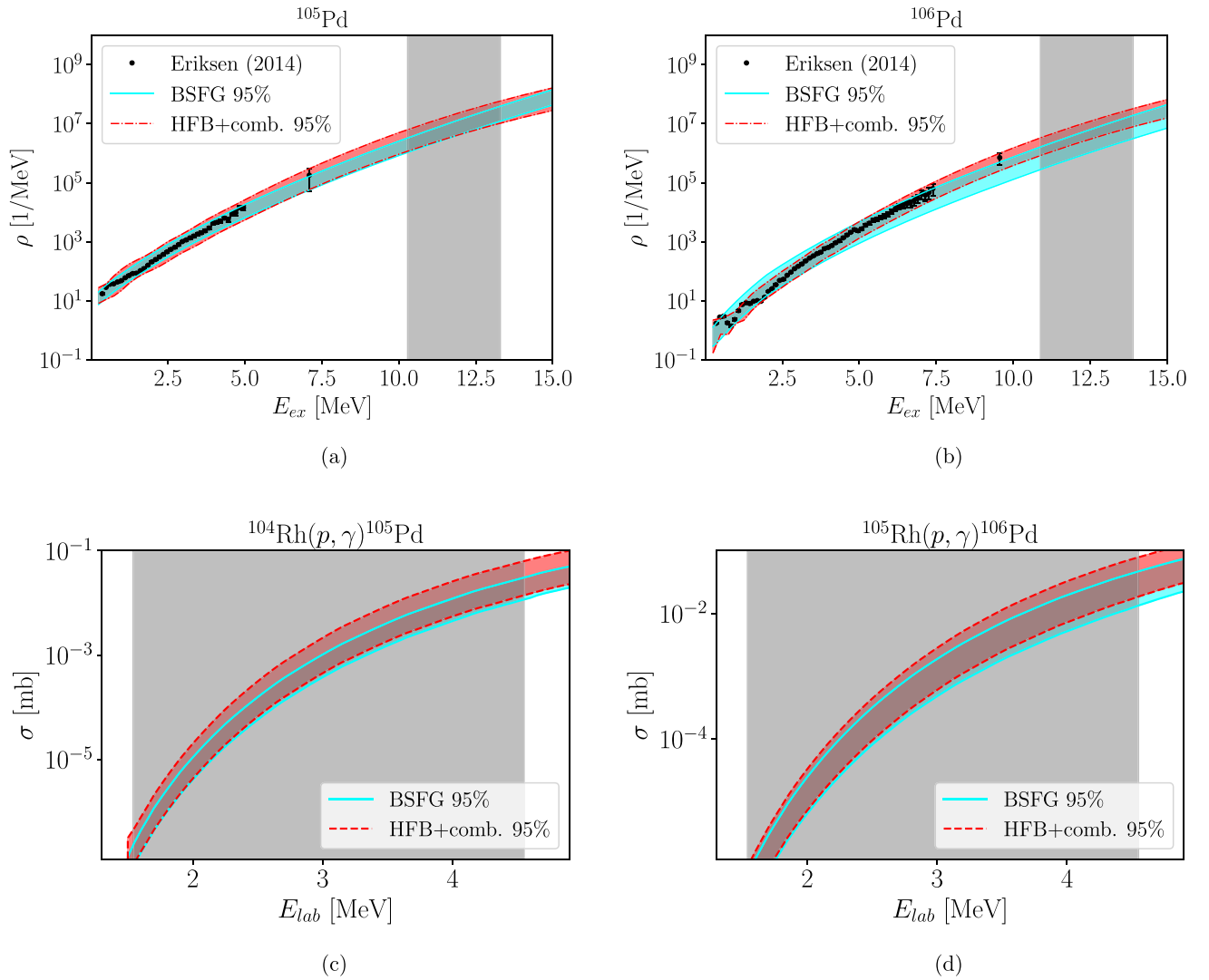


FIG. 3. Calculated level densities and cross sections using the posterior distributions of the parameters  $a$ ,  $\delta^{\text{BSFG}}$  and  $f^{\text{BSFG}}$  of the BSFG model and the parameters  $a$ ,  $\delta^{\text{HFB}}$  and  $f^{\text{HFB}}$  of the HFB + comb model for the isotopes  $^{105,106}\text{Pd}$ . The 95% credible intervals obtained after Bayesian optimization are shown with the cyan and red bands, for the BSFG and HFB + comb models, respectively. The gray-shaded area represents the Gamow window for the reactions  $^{104,105}\text{Rh}(p, \gamma)^{105,106}\text{Pd}$ . See text for details.

in Figs. 4(c) and 4(d), following a similar trend as the NLD uncertainties.

### C. Prior sensitivity and autocorrelation

It is useful for every study using Bayesian inference to include a sensitivity study of the posterior distribution due to the prior distribution. An efficient way to check this sensitivity is described in Ref. [40] and consists of checking the posterior distribution by varying the standard deviation of the Gaussian priors.

In Fig. 5, the posterior 95% credible intervals for the parameters  $a$  and  $\delta^{\text{BSFG}}$  of the BSFG model are shown as a function of the standard deviation of their Gaussian priors. The sensitivity check starts from a Gaussian distribution with mean,  $\mu$ , equal to the systematic values of level densities and a standard deviation equal to  $\lambda \times a_M$ ,  $\delta_M^{\text{BSFG}}$  for  $a$  and  $\delta^{\text{BSFG}}$ , respectively. The standard deviation of the prior can

then be varied by increasing the factor  $\lambda$ , that is, by increasing the width of the Gaussians. As shown in Fig. 5, for  $\lambda < 1$ , there seems to be a strong variation of the posterior as a function of the standard deviation of the prior. After this threshold, the posteriors seem to be the same, something that is expected as the prior becomes too uninformative. In all calculations presented in this work, the factor  $\lambda$  is chosen large enough ( $\lambda = 100$ ) in order to minimize prior influence and fully explore the parameter space, as argued in Ref. [45].

The memory effect (autocorrelation) of the Markov Chain can be solved by running a large chain or thinning the chain by a step. In Fig. 6, the trace of the parameter  $a$  of the BSFG is shown for the isotope  $^{106}\text{Cd}$ . The traces of the rest of the parameters for all the cases studied in the present work exhibit similar behavior. A chain of 10 000 events was run using six walkers. As shown, no correlating structure is viewed in the trace.

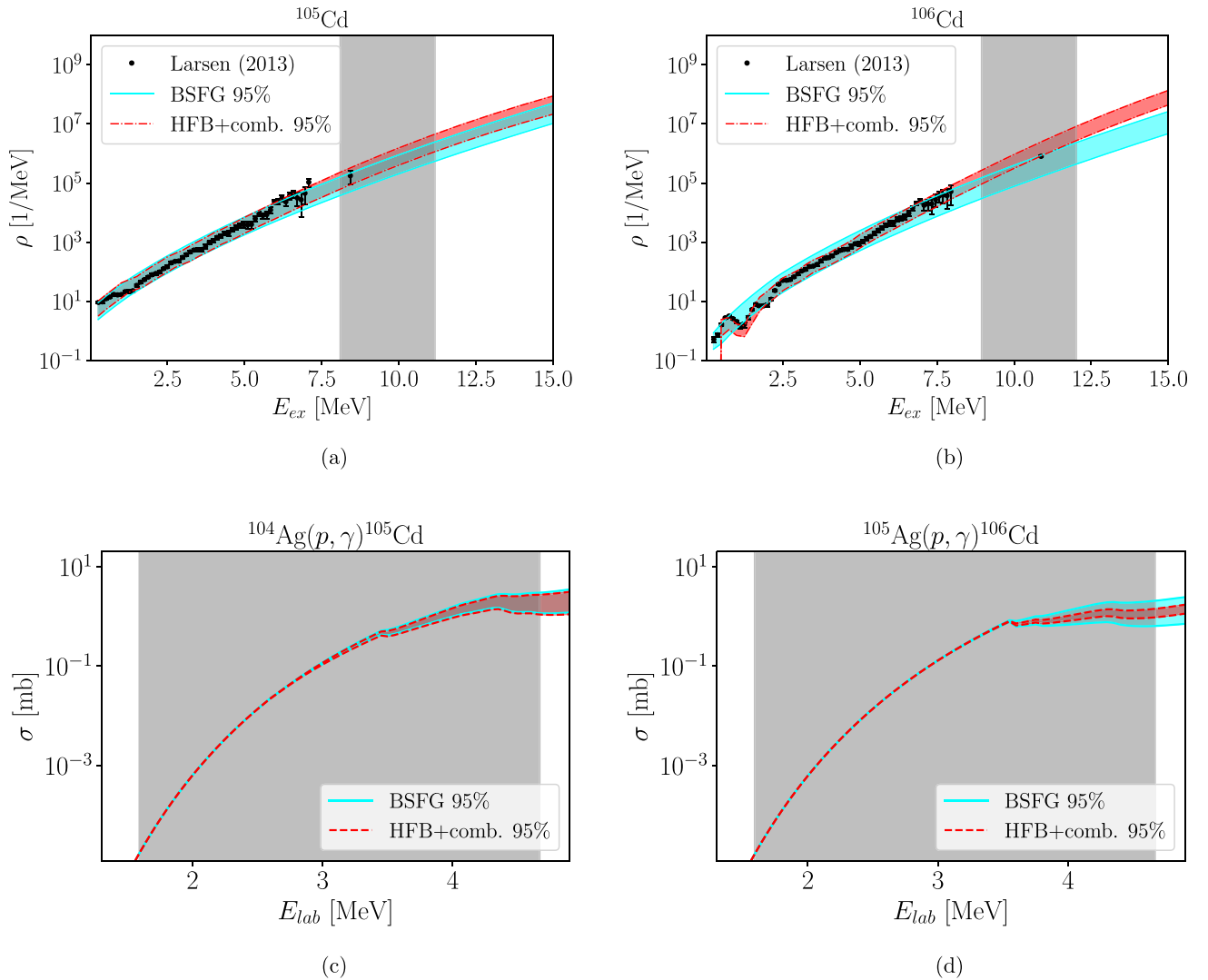


FIG. 4. Calculated level densities and cross sections using the posterior distributions of the parameters  $a$ ,  $\delta^{\text{BSFG}}$  and  $f^{\text{BSFG}}$  of the BSFG model and the parameters  $a$ ,  $\delta^{\text{HFB}}$  and  $f^{\text{HFB}}$  of the HFB + comb model for the isotopes  $^{105,106}\text{Cd}$ . The 95% credible intervals obtained after Bayesian optimization are shown with the cyan and red bands, for the BSFG and HFB + comb models, respectively. The gray-shaded area represents the Gamow window for the reactions  $^{104,105}\text{Ag}(p, \gamma)^{105,106}\text{Cd}$ . See text for details.

#### D. Comparison with all TALYS models

A comparison with the range of all available default TALYS models has also been performed in order to compare the ranges of cross sections for the case of reaction  $^{105}\text{Ag}(p, \gamma)^{106}\text{Cd}$ . The results are compared with the 95% confidence levels that were calculated using the level-density data and the BSFG and HFB + comb models. The comparison is shown in Fig. 7.

The range between the maximum and minimum of all six default TALYS models can cover a relatively large range which can reach a difference of 1.5 mb for the higher energies in the Gamow window. With the use of level-density data, this uncertainty interval is significantly reduced to approximately 0.5 mb for the HFB + comb model. This highlights the importance of the level-density data in constraining important cross sections for the  $p$  process. It has to be noted however that extrapolation to the Gamow window is necessary, as there

are usually no level-density data at such excitation energies. This can pose significant challenges in constraining the cross sections and highlights the need for both level-density and cross-section data inside the Gamow window.

#### IV. CONCLUSIONS AND FUTURE DIRECTIONS

Four important radiative proton-capture reactions within the  $p$  process reaction have been studied by using Bayesian inference in order to quantify the uncertainties that arise from measured level-density data. The 95% credible intervals using the normalized level-density data from the OSLO database [20] have been calculated and propagated to the  $(p, \gamma)$  cross sections. While the present study is oriented on the cross sections of proton-capture reactions of astrophysical interest, uncertainties in level densities could also constrain other observables in different domains such as in fission [51].



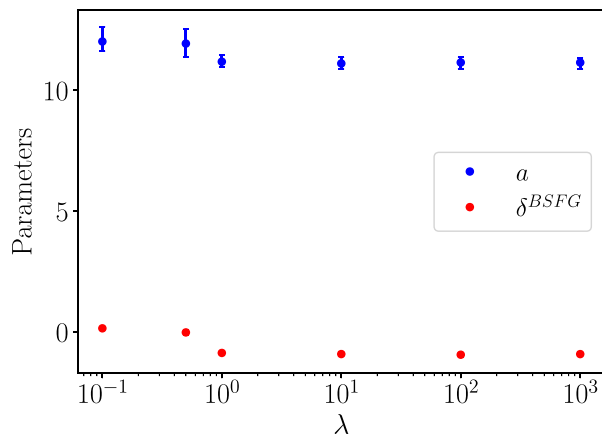


FIG. 5. Prior sensitivity of posterior distributions for the parameters  $a$  and  $\delta^{BSFG}$  of the BSFG for the isotope  $^{106}\text{Cd}$ . The standard deviation of the Gaussian prior is given by the product of the factor  $\lambda$  and the mean of the Gaussian prior. For large values of  $\lambda$ , the prior distributions becomes more wide (uninformative prior), stabilizing the posterior to specific values. Error bars represent the 95% credible intervals of the posteriors. See text for details.

In three out four cases studied in the present work, the HFB + comb model seems to provide smaller credible intervals. An exception seems to be the case of  $^{105}\text{Cd}$ , where uncertainties were found smaller by using the BSFG model. This indicates that different models can give different results when optimized on the same dataset, making the choice of the model important. In all cases though, the shape of the credible intervals of the HFB + comb model seem to describe very well the low-energy level densities.

The level densities are not the only factor that affects the final proton-capture cross section. The optical model potential and the  $\gamma$ -strength function have also a significant impact. A Bayesian approach has already been used for the  $\gamma$ SF for the reaction  $^{93}\text{Nb}(p, \gamma)^{94}\text{Mo}$ , by using the OSLO data [52]. It is important to note, that no large scale uncertainty quantification study has been made on the proton-nucleus OMPs. Although these OMPs seem in general to describe

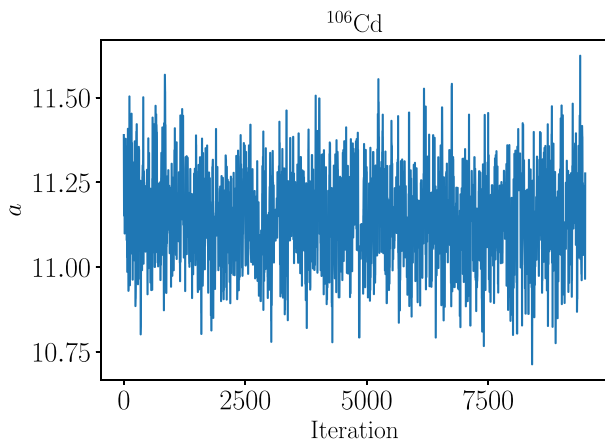


FIG. 6. Trace of the parameter  $a$  of the BSFG for the nucleus  $^{106}\text{Cd}$ .

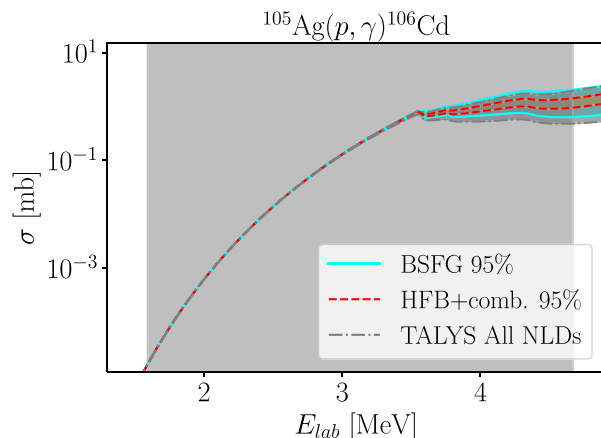


FIG. 7. Cross sections calculations comparing the range of all six default TALYS level-density models with the Bayesian 95% credible intervals of the BSFG and HFB + comb models for  $^{106}\text{Cd}$ . See text for details.

well the experimental data in the lower part of the Gamow window [24,25,53,54], there exist cases in which they do not give a good description in the whole energy range [10]. In combination with the present work on NLDs, Bayesian uncertainty quantification on the proton-OMP and  $\gamma$ SF models could give a more complete picture on the cross sections uncertainties.

Constraining radiative capture cross sections is highly important for the  $p$  process reaction network. The present results can serve as a reference for both theoretical and experimental future works. Combined with further uncertainty quantification studies, by taking advantage of the existing data on OMPs, NLDs,  $\gamma$ SFs, such studies could give insight on the values of the relevant cross sections and reaction rates where experimental information directly on the cross section is challenging. Uncertainties could then be propagated to the relevant reaction rates for network calculations and give significant insights on the origin of the  $p$  nuclei.

While this work is focused on proton-capture reactions, the impact of  $\alpha$  captures is also significant for the  $p$  process network. In this case, we have also to deal with the  $\alpha$ -nucleus potential problem, whose central value is not as well constrained as the nucleon-nucleus potentials. A Bayesian study on existing data could give insight on the uncertainties related to the  $\alpha$  optical potential, which is important in particular for the heavier  $p$  nuclei.

## ACKNOWLEDGMENTS

The authors thank the anonymous reviewer, whose constructive comments have significantly contributed to the improvement of the present work. The authors are grateful to the LABEX Lyon Institute of Origins (ANR-10-LABX-0066) Lyon for its financial support within the Plan France 2030 of the French government operated by the National Research Agency (ANR). A.C. is grateful to Dr. V. Lapoux, for the useful discussions over the present work.

- [1] E. M. Burbidge, G. R. Burbidge, W. A. Fowler, and F. Hoyle, *Rev. Mod. Phys.* **29**, 547 (1957).
- [2] A. G. W. Cameron, *Publ. Astron. Soc. Pac.* **69**, 201 (1957).
- [3] A. Koloczek, B. Thomas, J. Glorius, R. Plag, M. Pignatari, R. Reifarh, C. Ritter, S. Schmidt, and K. Sonnabend, *At. Data Nucl. Data Tables* **108**, 1 (2016).
- [4] S. J. Smartt, T.-W. Chen, A. Jerkstrand, M. Coughlin, E. Kankare, S. A. Sim, M. Fraser, C. Inerra, K. Maguire, K. C. Chambers *et al.*, *Nature (London)* **551**, 75 (2017).
- [5] N. Domoto, M. Tanaka, S. Wanajo, and K. Kawaguchi, *Astrophys. J.* **913**, 26 (2021).
- [6] M. Arnould and S. Goriely, *Phys. Rep.* **384**, 1 (2003).
- [7] M. Rayet, M. Arnould, M. Hashimoto, N. Prantzos, and K. Nomoto, *Astron. Astrophys.* **298**, 517 (1995).
- [8] C. Travaglio, F. K. Röpké, R. Gallino, and W. Hillebrandt, *Astrophys. J.* **739**, 93 (2011).
- [9] A. Choplin, S. Goriely, R. Hirschi, N. Tominaga, and G. Meynet, *Astron. Astrophys.* **661**, A86 (2022).
- [10] A. Psaltis, A. Khaliel, E.-M. Assimakopoulou, A. Kanellakopoulos, V. Lagaki, M. Lykiardopoulou, E. Malami, P. Tsavalas, A. Zyriliou, and T. J. Mertzimekis, *Phys. Rev. C* **99**, 065807 (2019).
- [11] G. Gyürky, Z. Fülöp, F. Käppeler, G. G. Kiss, and A. Wallner, *Eur. Phys. J. A* **55**, 41 (2019).
- [12] A. Spyrou, H.-W. Becker, A. Lagoyannis, S. Harissopulos, and C. Rolfs, *Phys. Rev. C* **76**, 015802 (2007).
- [13] G. Lotay, S. A. Gillespie, M. Williams, T. Rauscher, M. Alcorta, A. M. Amthor, C. A. Andreou, D. Baal, G. C. Ball, S. S. Bhattacharjee *et al.*, *Phys. Rev. Lett.* **127**, 112701 (2021).
- [14] P. Ujčić, A. Lagoyannis, T. J. Mertzimekis, F. de Oliveira Santos, S. Harissopulos, P. Demetriou, L. Perrot, C. Stodel, M. G. Saint-Laurent, O. Kamalou *et al.*, *AIP Conf. Proc.* **1377**, 321 (2011).
- [15] W. Hauser and H. Feshbach, *Phys. Rev.* **87**, 366 (1952).
- [16] W. Rapp, J. Görres, M. Wiescher, H. Schatz, and F. Käppeler, *Astrophys. J.* **653**, 474 (2006).
- [17] M. Guttormsen, T. Tvetter, L. Bergholt, F. Ingebretsen, and J. Rektstad, *Nucl. Instrum. Methods A* **374**, 371 (1996).
- [18] T. Rauscher, A. Heger, R. D. Hoffman, and S. E. Woosley, *Astrophys. J.* **576**, 323 (2002).
- [19] T. Rauscher, N. Dauphas, I. Dillmann, C. Fröhlich, Z. Fülöp, and G. Gyürky, *Rep. Prog. Phys.* **76**, 066201 (2013).
- [20] Level densities and gamma-ray strength functions, <https://www.mn.uio.no/fysikk/english/research/about/infrastructure/ocl/nuclear-physics-research/compilation/> (accessed 2023).
- [21] A. Spyrou, A. Lagoyannis, P. Demetriou, S. Harissopulos, and H.-W. Becker, *Phys. Rev. C* **77**, 065801 (2008).
- [22] S. Harissopulos, A. Spyrou, V. Foteinou, M. Axiotis, G. Provatias, and P. Demetriou, *Phys. Rev. C* **93**, 025804 (2016).
- [23] T. K. Eriksen, H. T. Nyhus, M. Guttormsen, A. Görger, A. C. Larsen, T. Renstrøm, I. E. Ruud, S. Siem, H. K. Toft, G. M. Tveten *et al.*, *Phys. Rev. C* **90**, 044311 (2014).
- [24] A. Khaliel, T. J. Mertzimekis, E.-M. Asimakopoulou, A. Kanellakopoulos, V. Lagaki, A. Psaltis, I. Psyrra, and E. Mavrommatis, *Phys. Rev. C* **96**, 035806 (2017).
- [25] F. Heim, P. Scholz, M. Körschgen, J. Mayer, M. Müller, and A. Zilges, *Phys. Rev. C* **101**, 035805 (2020).
- [26] A. C. Larsen, I. E. Ruud, A. Bürger, S. Goriely, M. Guttormsen, A. Görger, T. W. Hagen, S. Harissopulos, H. T. Nyhus, T. Renstrøm *et al.*, *Phys. Rev. C* **87**, 014319 (2013).
- [27] W. Dilg, W. Schantl, H. Vonach, and M. Uhl, *Nucl. Phys. A* **217**, 269 (1973).
- [28] M. Grossjean and H. Feldmeier, *Nucl. Phys. A* **444**, 113 (1985).
- [29] S. Goriely, S. Hilaire, and A. J. Koning, *Phys. Rev. C* **78**, 064307 (2008).
- [30] C. Iliadis, *Nuclear Physics of Stars* (Wiley, New York, 2007).
- [31] A. J. Koning, S. Hilaire, and M. C. Duijvestijn, in *Proceedings of the International Conference on Nuclear Data for Science and Technology* (2007), pp. 211–214.
- [32] A. Koning and J. Delaroche, *Nucl. Phys. A* **713**, 231 (2003).
- [33] J. Kopecky and M. Uhl, *Phys. Rev. C* **41**, 1941 (1990).
- [34] S. Goriely, A.-C. Larsen, and D. Mücher, *Phys. Rev. C* **106**, 044315 (2022).
- [35] T. von Egidy and D. Bucurescu, *Phys. Rev. C* **72**, 044311 (2005).
- [36] M. Wiedeking, M. Guttormsen, A. C. Larsen, F. Zeiser, A. Görger, S. N. Liddick, D. Mücher, S. Siem, and A. Spyrou, *Phys. Rev. C* **104**, 014311 (2021).
- [37] P. E. Hodgson, *Rep. Prog. Phys.* **50**, 1171 (1987).
- [38] G. Satchler, *Introduction to Nuclear Reactions* (Oxford University Press, Oxford, 1990).
- [39] A. J. Libert and A. G. W. Cameron, *Can. J. Phys.* **43**, 1446 (1965).
- [40] A. E. Lovell and F. M. Nunes, *Phys. Rev. C* **97**, 064612 (2018).
- [41] M. Catacora-Rios, G. B. King, A. E. Lovell, and F. M. Nunes, *Phys. Rev. C* **104**, 064611 (2021).
- [42] T. R. Whitehead, T. Poxon-Pearson, F. M. Nunes, and G. Potel, *Phys. Rev. C* **105**, 054611 (2022).
- [43] M. Catacora-Rios, A. E. Lovell, and F. M. Nunes, *Phys. Rev. C* **108**, 024601 (2023).
- [44] C. Hebborn, F. M. Nunes, and A. E. Lovell, *Phys. Rev. Lett.* **131**, 212503 (2023).
- [45] G. B. King, A. E. Lovell, L. Neufcourt, and F. M. Nunes, *Phys. Rev. Lett.* **122**, 232502 (2019).
- [46] J. Goodman and J. Weare, *Commun. Appl. Math. Comput. Sci.* **5**, 65 (2010).
- [47] D. Foreman-Mackey, D. W. Hogg, D. Lang, and J. Goodman, *Publ. Astron. Soc. Pac.* **125**, 306 (2013).
- [48] See Supplemental Material at <http://link.aps.org/supplemental/10.1103/PhysRevC.110.024602> for a Python connector script.
- [49] D. W. Hogg, J. Bovy, and D. Lang, Data analysis recipes: Fitting a model to data, [arxiv:1008.4686v1](https://arxiv.org/abs/1008.4686v1).
- [50] Fitting a model to data, emcee documentation, <https://emcee.readthedocs.io/en/stable/tutorials/line/>.
- [51] V. Piau, O. Litaize, A. Chebboubi, S. Oberstedt, A. Göök, and A. Oberstedt, *Phys. Lett. B* **837**, 137648 (2023).
- [52] F. Heim, P. Scholz, J. Mayer, M. Müller, and A. Zilges, *Phys. Rev. C* **101**, 035807 (2020).
- [53] S. Harissopulos, E. Vagena, P. Dimitriou, M. Axiotis, S. Galanopoulos, V. Foteinou, and A. Lagoyannis, *Phys. Rev. C* **104**, 025804 (2021).
- [54] A. Palmisano-Kyle, A. Spyrou, P. A. DeYoung, A. Dombos, P. Gastis, O. Olivas-Gomez, C. Harris, S. Liddick, S. M. Lyons, J. Pereira *et al.*, *Phys. Rev. C* **105**, 065804 (2022).